# THE EFFECT OF A COMPOSITE CHITOSAN-SILVER(I) ION COATING ON THE CORROSION RESISTANCE OF THE COBALT-CHROMIUM-MOLYBDENUM ALLOY IN SALINE SOLUTION

**Bożena Łosiewicz[1,a,*], Patrycja Osak[1,b], Julian Kubisztal[1,c]**

*[1] – Institute of Materials Engineering, Faculty of Science and Technology, University of Silesia in Katowice, 75 Pułku Piechoty 1A Str., 41–500 Chorzów, Poland*
*[a] – ORCID: 0000–0001–9472–1893, [b] – ORCID: 0000–0002–0628–6367,*
*[c] – ORCID: 0000–0002–4855–9538*
*[*] corresponding author: bozena.losiewicz@us.edu.pl*

## Abstract

*We determined the in vitro corrosion resistance of the composite chitosan-silver(I) [Ag(I)] ion coating on the cobalt-chromium-molybdenum (CoCrMo) dental alloy in a 0.9% sodium chloride (NaCl) solution at 37°C. We obtained the novel composite chitosan–Ag(I) ion coating by electrophoretic deposition at 20 V for 30 s at room temperature in a 2% (v/v) aqueous solution of acetic acid with 1 g $dm^{-3}$ chitosan and 10 g $dm^{-3}$ silver nitrate. We evaluated the chemical composition with energy dispersive spectroscopy and Fourier-transform infrared spectroscopy. We investigated surface topography and electronic properties with a scanning Kelvin probe. We determined the mechanism and kinetics of the electrochemical corrosion of the obtained coatings by electrochemical impedance spectroscopy. The Ag content in the composite chitosan–Ag(I) ion coating was 1.9 ± 1 wt.%. The cataphoretic co-deposition of chitosan and Ag(I) ions in an aqueous solution can be used to modify the CoCrMo alloy surface to obtain new coatings with antibacterial properties.*

***Keywords:*** *chitosan, CoCrMo alloy, composite, corrosion resistance, dentistry, silver*

**Received:** 20.03.2023
**Accepted:** 05.06.2023

## 1. Introduction

Metallic materials are the largest group of biomaterials used in dental prosthetics as well as in maxillofacial surgery and orthodontics [1, 2]. In dental prosthetics, mainly precious and base metals and their alloys are applied. Precious metals, such as gold and platinum [3–5], have been used for many years in dental prosthetics, but for economic reasons their use has been significantly limited been replaced by titanium [6–10] and base metal alloys [11–27]. The currently used cobalt alloys can be divided into casting Vitallium alloys, wrought alloys, and powder metallurgy alloys [28, 29]. Cobalt alloys are characterised by good biocompatibility, low thermal conductivity, a high modulus of elasticity, high strength, a short cooling time after casting, a low coefficient of thermal expansion, and high resistance to corrosion [26–29]. Cobalt-based alloys are among the materials with good biotolerance, resulting from the presence of a passive oxide layer on their surface. This layer is mainly formed by chromium(III) oxide, which is formed spontaneously. Cobalt alloys show greater biocompatibility in the environment of tissues and body fluids, as well as greater resistance to pitting, crevice and fatigue corrosion in comparison to austenitic CrNiMo steel and Ti6Al4V alloy [26–29].

Dental prosthetics have improved over time with the continuous development of more effective solutions to improve the health and quality of life of patients, especially considering the ageing of the global population. New biomaterials with even greater biocompatibility and better immune system tolerance are constantly sought. Of great interest are biodegradable polymers of natural origin, which include polysaccharides [30–41]. Due to their similarity to the extracellular matrix, natural polymers do not induce the toxic effects of the immune system. Chitosan (CS) is a natural polysaccharide that is often used in medicine; it is composed of simple sugar molecules connected by glycosidic bonds [31, 32, 34]. Figure 1 shows the structure of CS obtained by chitin deacetylation. CS is a linear polysaccharide composed of randomly distributed β–(1→4)–linked D–glucosamine (deacetylated unit) and *N*–acetyl–D–glucosamine (acetylated unit). There are three reactive groups in CS, namely an amino group at the C2 position and primary and secondary –OH groups at the C3 and C6 positions.

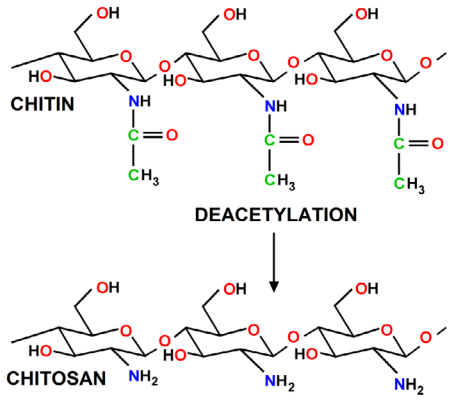


**Figure 1.** The structure of chitin and chitosan.

CS is non-toxic, biocompatible, and biodegradable. It has antibacterial, anti-inflammatory, and analgesic effects [32, 41]. CS stops bleeding and accelerates wound healing; these properties make it useful as a dressing material. It is the most common polymer of natural origin, obtained by chemical deacetylation of chitin from the shells of red crabs, shrimp, krill, and other crustaceans, as well as from fungi [31]. CS is used to obtain polymer gels

and porous structures for drug delivery, artificial skin, and contact lens applications [32, 34, 40]. It can also be obtained in the form of coatings on metallic dental materials [31, 35–38]. The cationic nature of CS allows protein structures to attach to it, stimulating a positive biological response. Recently, CS has been used to immobilise silver (Ag) particles [30, 33]. This antimicrobial additive agent has been co-deposited with the CS matrix in the ionic form and as micro- or nanoparticles. In one study, researchers reported that the antibacterial properties of composite CS–Ag coatings are dependent on size, concentration, temperature, and ionic strength of Ag(I) micro- or nanoparticles. However, there are difficulties in controlling the size, shape, and agglomeration effects of Ag particles in composite component [33].

We focused on the development of a method for the production of the CS–Ag(I) ion composite coating deposited on the cobalt–chromium–molybdenum (CoCrMo) dental alloy using new conditions for electrophoretic deposition (EPD). We propose a simple and environmentally friendly *in situ* chemical synthesis to stabilise Ag(I) in the CS matrix. This is the first study on the effect of the novel CS–Ag(I) ion coating on the electronic and anti-corrosive properties of the CoCrMo alloy in a physiological saline (0.9% sodium chloride [NaCl]) solution. We performed preliminary tests using a scanning Kelvin probe (SKP) and open circuit potential (OCP) method combined with electrochemical impedance spectroscopy (EIS). Because there is still a lack of detailed information concerning the mechanism and kinetics of pitting corrosion of the CoCrMo alloy at the atomic level, we applied the appropriate equivalent electrical circuit for the pitting corrosion.

## 2. Materials and Methods

### 2.1. Substrate Preparation

The CoCrMo alloy – chemical composition (at.%) Co 63.0, Cr 30.0, and Mo 5.0 (Si, Mn < 2) – was purchased from Bego (Germany) in the form of cylinders from which samples (6 mm in diameter and 3 mm thick) were cut. The disc-shaped samples were ground with 600# to 5000# silicon carbide paper and then polished on felt using a small amount of a suspension of $SiO_2$ with a grain size of 0.1 μm (OP–S, Struers Inc., USA) using a metallographic grinding and polishing machine (Forcipol 102, Metkon Instruments Inc., Turkey). The prepared samples were washed with ultra-pure water (Millipore, resistivity 18.2 MΩ cm) and acetone for 20 min in an ultrasonic cleaner to remove undesirable impurities. The washing was repeated twice. Each electrode with a geometric surface area of 0.503 $cm^2$ was prepared by ensuring electrical contact using insulated copper wire attached to the back of the CoCrMo discs with silver resin. The back and sides of the electrodes were covered with a chemically resistant, two-component epoxy resin. Prior to EPD, the electrodes were immersed in a hydrochloric acid (HCl) solution to remove the oxide layer from the substrate surface.

### 2.2. EPD Parameters

Polymer CS coating was deposited cataphoretically onto the CoCrMo substrate from a 2% (v/v) aqueous solution of acetic acid ($CH_3COOH$) containing 1 g $dm^{-3}$ CS. The solvent was Millipore water. The solutions were magnetically stirred at 300 rpm for 24 h until the CS powder was completely dissolved. The molecular weight of CS was 80 kDa and the degree of deacetylation was 75%–85%. All reagents used were purchased from Sigma-Aldrich (USA).

For EPD of the composite CS–Ag(I) ion coating, a 2% (v/v) aqueous solution of $CH_3COOH$ was prepared, in which 1 g $dm^{-3}$ CS and 10 g $dm^{-3}$ silver nitrate ($AgNO_3$) were dissolved. The EPD solution was sonicated for 30 min at room temperature. The CS and

composite CS–Ag(I) ion coatings were deposited at 20 V for 30 s at room temperature using a PWR800H high-current power supply (Kikusui Electronics Corporation, Japan). A two-electrode electrolytic cell was used with the CoCrMo cathode located face-to-face with the platinum anode at a distance of 1.5 cm. After EPD, each cathode was rinsed with Millipore water, air-dried for 24 h, and the weight gain was determined gravimetrically.

### 2.3. Chemical Composition Measurements

The local chemical composition was evaluated with a Hitachi TM4000 benchtop (Japan) scanning electron microscope with a tungsten cathode, equipped with an energy dispersive spectroscopy (EDS) detector by Oxford Instruments (UK) with AZtecOne analytical software. EDS spectra were collected from different homogeneous sample locations with a single scan area of $10 \times 10$ μm$^2$.

Identification of characteristic functional groups for CS powder, the polymer CS coating, and the composite CS–Ag(I) ion coating was determined by attenuated total reflectance Fourier-transform infrared (ATR-FTIR) spectroscopy. The ATR-FTIR absorption spectra were collected over the 4000–400 cm$^{-1}$ spectral range at 100 scans per sample at 21 ± 1 °C. A Trace-100 IR spectrophotometer from Shimadzu (Japan) was equipped with an ATR attachment with a diamond for examining solids.

### 2.4. Surface Topography and Electronic Property Measurements

The surface topography and electronic properties of the obtained materials were determined with a SKP in the air. The M370 scanning electrochemical workstation (Prinston Applied Research, USA) with the built-in SKP370 module and the VCAM3 optical video microscope was used. The U-SKP-150 tungsten microprobe (Uniscan Instruments, UK) was used, which consisted of a brass housing and a tungsten wire with a diameter of 150 μm. The tungsten microprobe tip was stable with a repeatable work function (WF), which ensured that the contact potential difference (CPD) did not change during the measurement due to the microprobe. The tip of the microprobe formed a parallel plate capacitor with the tested sample, enabling the measurement of the local CPD, which is the contact voltage between the surface of the two conductors [42]. An air gap was also used between the housing and the wire, which acted as a screen to reduce stray capacitance and to improve signal quality. The distance between the microprobe tip and the surface of the conductive sample was about 100 μm. A $2.5 \times 2$ mm$^2$ area was scanned. Non-contact measurement of surface topography maps and determination of changes in the CPD distribution on the surface of the tested materials was carried out in the height tracking mode. The tungsten microprobe moved over the sample surface in a sweep scan mode with a velocity of 20 μm s$^{-1}$. The data were recorded and analysed with the Scanning Electrochemical Work Station M370 Version 2.45 software.

### 2.5. Electrochemical Measurements

The CoCrMo alloy was tested before and after surface modification in a physiological saline solution deaerated with argon at pH 7.4 ± 1 and 37 ± 1 °C according to ISO 10271:2021–02 [43]. Electrochemical evaluations were conducted in a three-electrode system. The working electrode (WE) was the material under study. The counter electrode (CE) was a platinum foil with a surface area of 8 cm$^2$. All potentials were measured relative to the reference electrode (RE) in the form of a saturated calomel electrode (SCE). A computer-controlled electrochemical system, Autolab/PGSTAT30 (Metrohm Autolab B.V., The Netherlands), was used to evaluate corrosion resistance. Figure 2 shows a schematic of the Autolab/PGSTAT30 electrochemical system consisting of a potentiostat/galvanostat and the data acquisition system with a single software package.

The ADC164 module provided the ability to measure analogue signals. The input sensitivity was controlled with software at ± 10, ± 1, and ± 0.1 V. Analogue signals were measured at a frequency of up to 60 kHz. The ADC module was used, among others, to measure the power of the voltage follower (VF) and current follower (CF) of the potentiostat/galvanostat module. Two digital-to-analogue converter (DAC) channels were used to control the analogue potentiostat/galvanostat input. The DAC signals were summed in a potentiostat and divided by 2. This signal was used to set the WE potential against the RE or the current against the CE. The DAC164 module generated the analogue output signals. The output was controlled with software at ± 10 V. The digital input and digital output (DIO) module provided the ability to control electrode arrays, motorburets, or other equipment. The potentiostat/galvanostat made it possible to apply constant potentials and to measure currents. The ranges of the current and other adjustable values were computer controlled. The General Purpose Electrochemical System (GPES) for Windows (version 4.9) software was used to record electrochemical measurements and to analyse the results.

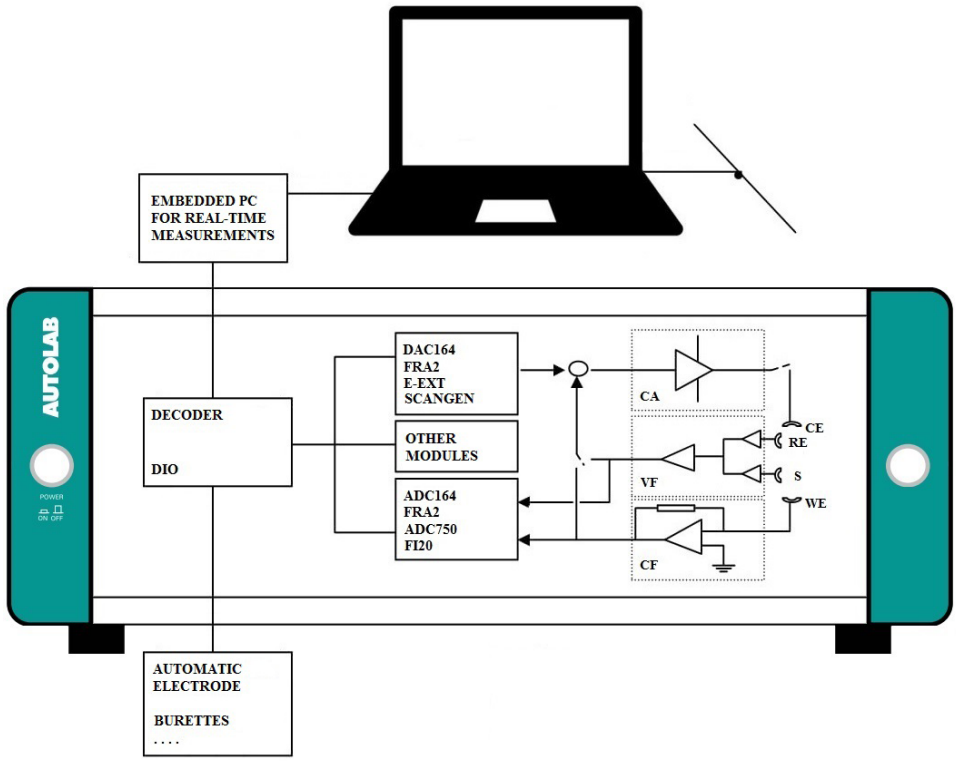


**Figure 2.** Scheme of the Autolab/PGSTAT30 electrochemical system.

According to ISO 10271:2021–02 [43], the open circuit potential ($E_{OC}$) was stabilised for 120 min. Next, the EIS measurements were conducted potentiostatically at the $E_{OC}$ and at the frequency range of 50 kHz to 1 mHz. The frequency resolution was 0.003%. Ten frequencies per decade were scanned using a sine-wave amplitude of 10 mV. Measurements in the time domain were analysed using the fast Fourier transform (FFT) method. Both the potential signal e(t) and the current signal i(t) were transformed to E(f), I(f), and their complex coupled forms E°(t) and I°(t). The cell impedance (Z) was calculated from Equation 1:

$$Z = \frac{E(f)E^{o}(f)}{I(f)E^{o}(f)}. \quad (1)$$

The correctness of the experimental EIS data was assessed using the Kramers-Kronig relations [44]. Ac impedance data were analysed with the EQUIVCRT program based on the concept of equivalent electrical circuits with the Boukamp description code using the complex non-linear least squares (CNLS) method [45]. The significance of the parameters used in the equivalent electrical circuits was checked using the F statistical test. Frequency Response Analyzer (FRA) for Windows (version 4.9) was used to measure the EIS spectra and to analyse the results. Three measurement series were performed for each electrode. The obtained value of each parameter is presented as the mean with the standard deviation.

## 3. Results and Discussion

### 3.1. Physical Properties of the Composite CoCrMo/CS-Ag(I) Ion Coating

Figure 3 presents surface topography maps recorded with the CoCrMo alloy before and after surface modification by EPD. The map of the surface topography of CoCrMo/CS shows four characteristic bulges with a diameter of 500–1000 μm. The bulges on the surface of the CS coating are the result of the electrolytic hydrogen evolution that accompanied EPD. On the map obtained for CoCrMo/CS–Ag(I), bulges are still visible, but they are the height is approximately 40% lower compared with CoCrMo/CS, which proves that Ag(I) as a surface modifier reduces the height of the bulge. The maximum peak height (the so-called Sp parameter) is about 3 times higher for CoCrMo/CS and about 2 times higher for CoCrMo/CS–Ag(I) compared with the pure alloy. Sp is 4.5, 14.0, and 8.6 μm, respectively, for CoCrMo, CoCrMo/CS, and CoCrMo/CS–Ag(I). The maximum pit depth (the so-called Sv parameter) for CoCrMo, CoCrMo/CS, and CoCrMo/CS–Ag(I) is 4.4, 3.4, and 6.5 μm, respectively. It can be seen that the maximum height of the peaks and valleys is comparable for the CoCrMo alloy. In the case of CoCrMo/CS, the height of the peaks is > 4 times higher than the valleys, and for CoCrMo/CS–Ag(I) the height of the peaks is only 1.3 times higher than the valleys, which suggests that Ag(I) embedding in the CS matrix evens out the surface of the material. The mean difference in the height from the mean plane (the so-called Sa parameter) is 1.5, 1.9, and 2.2 μm for CoCrMo, CoCrMo/CS, and CoCrMo/CS–Ag(I), respectively. The CS coating and the addition of Ag(I) increase the heights of the peaks and valleys by approximately 1.2 and 1.4 times, respectively, compared with the CoCrMo alloy.

The arithmetic mean CPD ($CPD_{av}$) obtained for CoCrMo is –0.57 V. Deposition of the CS coating reduces the $CPD_{av}$ to 0.25 V. The $CPD_{av}$ for CoCrMo/CS is –0.82 V, which means that the CS coating has worse protective properties compared with CoCrMo in air. The addition of Ag(I) significantly increases the $CPD_{av}$ by about 0.5 V compared with CoCrMo/CS and by about 0.27 V compared with the pure alloy. $CPD_{av}$ for CoCrMo/CS–Ag(I) is –0.30 V. This means that the addition of Ag(I) should reduce the activity of the CS coating in air.

The mean difference in CPD values from the mean plane ($CPD_a$) for CoCrMo, CoCrMo/CS, and CoCrMo/CS–Ag(I) is 83, 25, and 23 mV, respectively. It follows that the pure alloy has a higher $CPD_a$ between 3.3 and 3.6 compared with CoCrMo/CS and CoCrMo/CS–Ag(I). The pure alloy is characterised by much greater variability in CPD compared with CoCrMo/CS and CoCrMo–CS–Ag(I), a phenomenon that may be related to the presence of a self-passive oxide layer with a heterogeneous structure. The fluctuation of the CPD around the average value for CoCrMo/CS and CoCrMo/CS–Ag(I) is comparable. It follows

that the CS coating and the composite CS–Ag(I) ion coating homogenise the electrical properties of the CoCrMo alloy surface. The variability in the CPD of the tested surfaces is a very sensitive indicator of surface phenomena related to modification of the surface of the CoCrMo alloy in air.

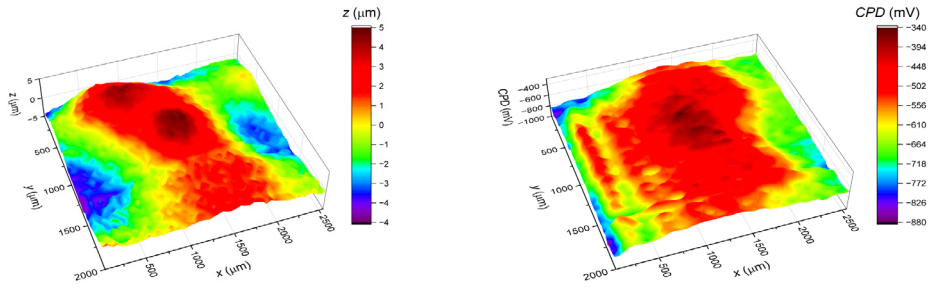


(a)

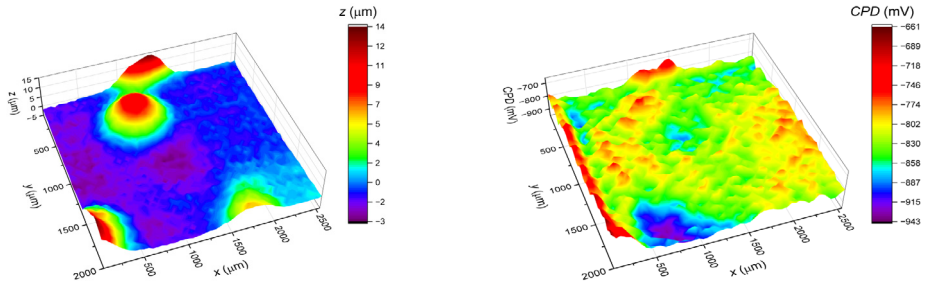


(b)

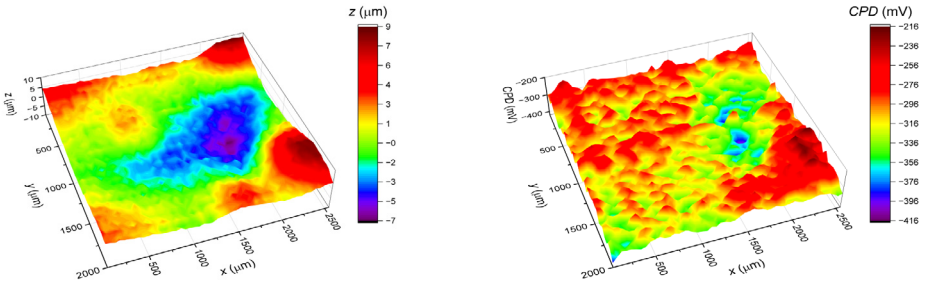


(c)

**Figure 3.** Surface topography map with the corresponding contact potential difference (CPD) map for (a) the CoCrMo substrate, (b) CoCrMo with the chitosan (CS) coating, and (c) CoCrMo with the CS-silver(I) [Ag(I)] ion coating.

CS is mucoadhesive and provides good coverage of wet surfaces and even mucous membranes. Microcrystalline CS is characterised by a high value of the secondary swelling indicator, a high adsorption capacity, and chelating abilities. EPD of the composite CS–Ag(I) ion coating on CoCrMo proceeds in two stages and is based on chelation of Ag(I) ions with CS. The first stage involves CS protonation, giving the CS macromolecules a positive charge, in a 2% (v/v) aqueous solution of $CH_3COOH$. CS amino groups are only protonated at pH < 6.5. Only under such conditions does CS become a cationic polyelectrolyte according to the reaction:

$$CS - NH_2 + H_3O^+ \rightarrow CS - NH_3^+ + H_2O. \quad (2)$$

The Ag(I) ions present in the solution interact with the protonated CS and CS–$NH_2Ag^+$ complexes form as follows:

$$CS - NH_3^+ + Ag^+ + H_2O \rightarrow CS - NH_2Ag^+ + H_3O^+. \quad (3)$$

During EPD, a dense and positively charged hydrogel coating forms on the cathode surface.

### 3.2. Chemical Composition of the Composite CoCrMo/CS-Ag(I) Ion Coating

EDS is a micro-analytical technique that conventionally uses scanning electron microscopy. We used it to determine the chemical elements in the composite CoCrMo/CS–Ag(I) ion coating. We confirmed the deposition of the composite CS–Ag(I) ion coating on the surface of the CoCrMo dental alloy by analysing the local chemical composition in homogeneous micro-areas. Figure 4 shows a representative EDS spectrum recorded from the CoCrMo/CS–Ag(I) surface with visible peaks of carbon (C), Ag, Co, Cr, and Mo.

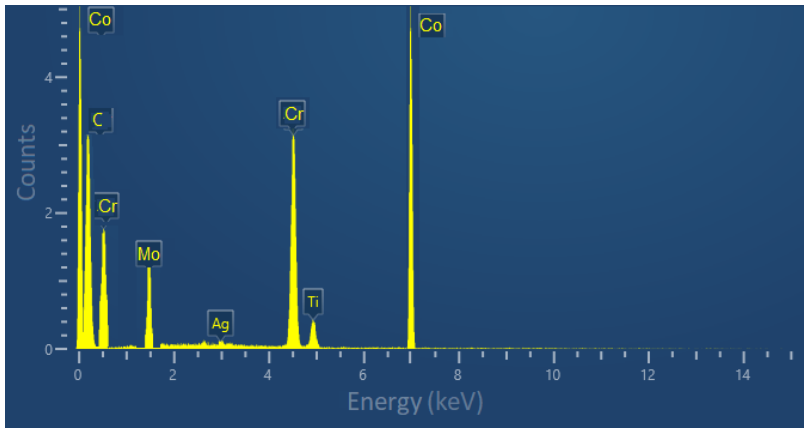


**Figure 4.** Energy-dispersive spectrum for the composite chitosan-silver(I) ion coating on the cobalt-chromium-molybdenum (CoCrMo) substrate.

The EDS analysis revealed the presence of C, which is the main element of the deposited CS matrix. The spectral lines originating from Ag confirm the presence of Ag(I) in the obtained composite coating. The Ag content in the composite CS–Ag(I) ion coating was 1.9 ± 1 wt.%. This amount of Ag provides maximum antibacterial activity of the CS-based coating. We also noted peaks from Co, Cr, and Mo as alloying elements in the substrate. However, the occurrence of peaks originating from the substrate is related to the depth of penetration of the electron beam. Based on scanning electron microscopic observations of cross-sections, we determined that the thickness of the composite CS–Ag(I) ion coating on CoCrMo was 20 ± 5 µm. Moreover, the thickness of the CS coating on CoCrMo was 13 ± 4 µm.

The ATR-FTIR measurements supported the EDS results. Figure 5 shows representative ATR-FTIR absorption spectra for the CS powder, the CS coating on CoCrMo, and the composite CoCrMo/CS–Ag(I) ion coating on CoCrMo. The CS powder spectrum shows the presence of peaks characteristic of polysaccharides. The peak at 3556 $cm^{-1}$ indicates symmetric stretching vibrations of the O–H and N–H bonds of the amine. There is a high-intensity peak at 2631 $cm^{-1}$, which is associated with the presence of $NH_2$

bonds characteristic of CS. The peaks at 1651 and 1025 $cm^{-1}$ indicate the occurrence of stretching vibrations of the C=O bond in amide I and stretching of the C–O–C bond in the glucosamine ring, respectively. The peaks at 1540 and 1420 $cm^{-1}$ correspond to N–H bond bending vibrations and $CH_3$ bond deformations, respectively. The peak at 1025 $cm^{-1}$ is related to the asymmetric stretching of the C–O–C bond in the polysaccharide ring. The surface of the CoCrMo alloy presents bands characteristic of CS. The presence of Ag in the composite CoCrMo/CS–Ag(I) ion coating is denoted by the disappearance of the C=O and C–O–C bonds, denoted by the loss of the 1420 and 665 $cm^{-1}$ bands, respectively.

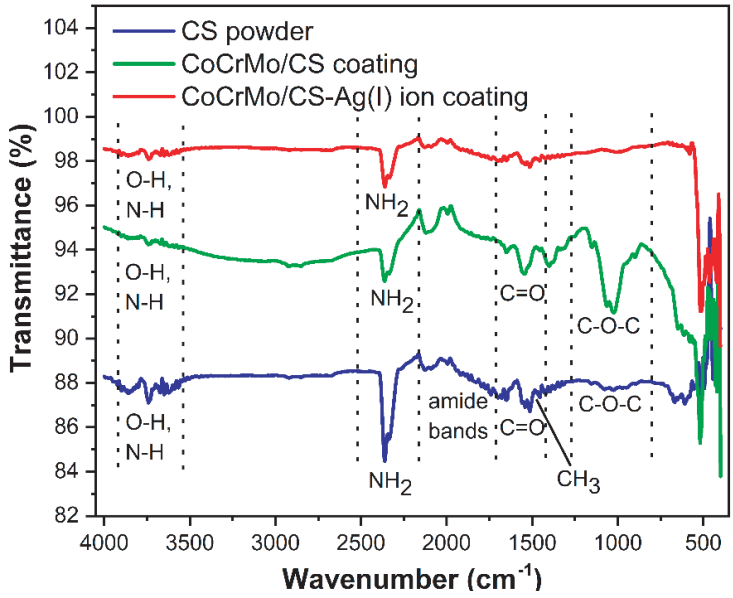


**Figure 5.** Attenuated total reflectance Fourier-transform infrared spectra for (a) chitosan (CS) powder, (b) cobalt-chromium-molybdenum (CoCrMo) with the CS coating, and (c) CoCrMo with the CS-silver(I) [Ag(I)] ion coating.

### 3.3. The Effect of Surface Modification on *In Vitro* Corrosion Resistance of the CoCrMo Alloy in Physiological Saline Solution

Considering that direct current methods cannot measure the charge transfer resistance ($R_{ct}$) at the metallic electrode-coating-electrolyte interface, we evaluated the kinetics and mechanism of electrochemical corrosion of the tested systems by using EIS. Figure 6 presents the results of *in vitro* EIS measurements for the CoCrMo electrode before and after EPD of the CS and composite CS–Ag(I) ion coatings in physiological saline solution at 37°C in the form of Bode diagrams. For all electrodes over the entire range of frequencies tested, there is only one semicircle with a diameter that is the largest for the CoCrMo electrode and the smallest for the electrode with the composite CS–Ag(I) ion coating. We fitted the experimental EIS spectra (symbols) using an equivalent electrical circuit of a modified Randle's cell with the Boukamp description code $R_1(R_2Q_1)$ and the CNLS method. In this equivalent electrical circuit representing the physical model of the CoCrMo electrode-coating-saline solution system, $R_1$ is the resistance of the solution, $R_2$ is the resistance of charge transfer through the coating-solution interface, and the electrical double layer capacitance parameter ($C_{dl}$) corresponds to the ideal capacitor. For the CNLS fitting procedure, instead of a capacitor we used the constant phase element (CPE) described in the Boukamp code as Q. Its impedance ($\hat{Z}_{CPE}$) is given by Equation 4, where

$T$ (in F cm$^{-2}$ s$^{\phi-1}$) is the capacitance parameter and $\phi \leq 1$ is a dimensionless CPE exponent related to the constant phase angle, $\alpha = 90°(1–\phi)$:

$$\hat{Z}_{\mathrm{CPE}} = \frac{1}{T(j\omega)^{\phi}}. \tag{4}$$

The Bode diagrams in the studied frequency range show a linear dependence of log |$Z$| on log $f$ with a slope close to –1 at the intermediate frequencies (Figure 6a), only one time constant, and a near-capacitive response (Figure 6b). One time constant in the circuit suggests that the corrosion process proceeds in one step via anodic dissolution. The maximum phase angle for the CoCrMo electrode with and without the CS coating is about –80°, while it is close to –70° for the CoCrMo/CS–Ag(I) electrode. A reduction in the phase angle indicates an increase in the conductivity of the tested electrodes with the deposited composite coating due to the presence of Ag(I). The parameters obtained using the $R_1(R_2Q_1)$ model shown in Figure 6a to fit the experimental EIS data for the CoCrMo electrode before and after surface modification in physiological saline solution at 37°C are presented in Table 1.

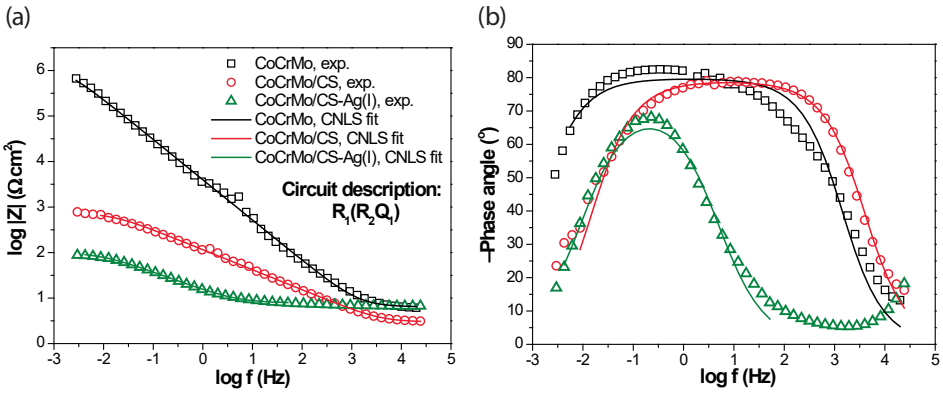


**Figure 6.** Experimental (symbols) and simulated (line) Bode diagrams: (a) log |$Z$| = f(log $f$) and (b) -$\phi$ = f(log $f$) for the cobalt-chromium-molybdenum (CoCrMo) electrode before and after deposition of the chitosan (CS) and composite CS-silver(I) [Ag(I)] ion coating in physiological saline solution at 37°C. The designations of the symbols and lines in panels a and b are the same.

**Table 1.** The parameters of the electrical equivalent circuit with their standard deviations obtained as a result of fitting the $R_1(R_2Q_1)$ model to the experimental electrical impedance spectroscopic data for the cobalt-chromium-molybdenum (CoCrMo) electrode before and after electrophoretic deposition in physiological saline solution at 37°C.

| Electrode type | $R_1$ [Ω cm$^2$] | $R_2$ [Ω cm$^2$] | $Q_1$–$T$ [F cm$^{-2}$ s$^{-1}$] | $Q_1$–$\phi$ |
|---|---|---|---|---|
| **CoCrMo** | 6.39 ± 0.30 | (1.43 ± 0.17)×10$^6$ | (1.38 ± 0.9)×10$^{-5}$ | 0.886 ± 0.006 |
| **CoCrMo/CS** | 4.50 ± 0.20 | (2.52 ± 0.15)×10$^5$ | (3.12 ± 0.7)×10$^{-5}$ | 0.877 ± 0.004 |
| **CoCrMo/CS–Ag(I)** | 29.70 ± 0.60 | (4.83 ± 0.17)×10$^3$ | (2.11 ± 0.3)×10$^{-3}$ | 0.812 ± 0.006 |

*Note.* Ag(I), silver(I); CS, chitosan.

The results of fitting presented in Table 1 for all tested materials indicate that the CoCrMo electrode had the highest corrosion resistance in saline solution. This electrode with a self-passive oxide layer and strong barrier properties has the highest value of $R_2$, a kinetic parameter of corrosion, specifically $(1.43 \pm 0.17) \times 10^6$ Ω cm$^2$. Modification of the CoCrMo alloy surface by depositing the CS and composite CS–Ag(I) ion coatings with antimicrobial properties did not improve the corrosion resistance, as evidenced by the $R_2$ value of $(2.52 \pm 0.15) \times 10^5$ and $(4.83 \pm 0.17) \times 10^3$ Ω cm$^2$, respectively. Along with the decrease in corrosion resistance, we observed an increase in the capacitive parameter $Q_1$–*T*. Such corrosion behaviour is caused by the nature of the coatings, which we prepared based on the hydrogel. CS-based biopolymer coatings absorb water in saline solution. The absorbed water may contribute to accelerate the gradual degradation of the biopolymer coating. CS degradation products that results from hydrolysis of bonds in CS and the tearing of individual polymer chains are removed from the body in the Krebs cycle. In the biological environment, the CS coating absorbs water and enzymes contained in it, succumbing to enzymatic degradation. As a result of the degradation of CS, Ag(I) ions are also released into the biological environment.

Corrosion of the CoCrMo alloy in a neutral saline solution is an electrochemical process whereby metal atoms are oxidised and released in the ionic form into a solution according to the following reactions:

$$Cr \rightarrow Cr^{3+} + 3e^-, \quad (5)$$

$$Co \rightarrow Co^{2+} + 2e^-, \quad (6)$$

$$Mo \rightarrow Mo^{2+} + 2e^-, \quad (7)$$

The electrons that are produced in the oxidation reaction must be consumed in a cathodic reaction such as the reduction of oxygen:

$$O_2 + 2H_2O + 4e^- \rightarrow 4OH^-, \quad (8)$$

or water reduction:

$$2H_2O + 2e^- \rightarrow H_2 + 2OH^-. \quad (9)$$

The value of the empirical parameter $Q_1$–$\phi$ for each tested electrode shows a significant deviation from 1 (Table 1). This phenomenon results from the presence of physical, chemical, or geometrical inhomogeneities on the surface of the tested electrodes.

## 4. Conclusions

Based on the obtained results, EPD can be used for the electrochemical production of the composite CS–Ag(I) ion coating on the CoCrMo dental alloy. The EDS and the ATR-FTIR analysis confirmed the deposition of the CS matrix and embedding of Ag(I) ions in the matrix. The composite CS–Ag(I) ion coating deposited under the proposed EPD conditions contained 1.9 ± 0.1 wt.%. of Ag(I) ions, which provides high antibacterial activity: a previous study reported that CS-based composites containing about 2 wt.% of Ag(I) have maximum antibacterial activity [33]. The surface topography maps recorded by the SKP method show the presence of characteristic bulges with a diameter of 500–1000 μm, which are related to the electrolytic hydrogen evolution that accompanies EPD. The SKP characterisation of the obtained coatings revealed that both the CS coating with a thickness of 13 ± 4 μm and the composite CS–Ag(I) ion coating with a thickness of 20 ± 5 μm homogenise the electrical properties of the CoCrMo alloy surface. We noted that the CoCrMo substrate has greater resistance to corrosion in physiological saline solution at 37ºC than the substrate with the CS or Cs–Ag(I) ion coating. The EIS evaluation of the

interfacial properties showed a capacitive behaviour for all tested electrodes. Only one time constant in the circuit suggests that the corrosion process proceeds in one step with slower kinetics in the case of the CoCrMo electrode. Water absorption by CS accelerates the degradation of CoCrMo/CS and CoCrMo/CS–Ag(I).

## 5. References


[1] Najman S, Mitić V, Groth T, Barbeck M, Chen P-Y, Sun Z, Randjelović B; (2023) Bioceramics, Biomimetic and Other Compatible Materials Features for Medical Applications. 1st ed, Springer Nature Switzerland AG, Cham.

[2] Motoyoshi M; (2022) Current Techniques and Materials in Dentistry. MDPI AG, Basel.

[3] Givan DA; (2014) Precious metal alloys for dental applications. In: Baltzer N, Copponnex T (eds), Precious Metals for Biomedical Applications. Woodhead Publishing, Cambridge, 109–129. **DOI:**10.1533/9780857099051.2.109

[4] Sinyakova EF, Vasilyeva IG, Oreshonkov AS, Goryainov SV, Karmanov NS; (2022) Formation of noble metal phases (Pt, Pd, Rh, Ru, Ir, Au, Ag) in the process of fractional crystallization of the $CuFeS_2$ melt. *Minerals 12, 1136*. **DOI:**10.3390/min12091136

[5] Rudolf R, Lazic V, Majeric P, Ivanic A, Kravanja G, Raic K; (2022) Dental Gold Alloys and Gold Nanoparticles for Biomedical Applications. Springer Nature Switzerland AG, Cham.

[6] Osak P, Maszybrocka J, Kubisztal J, Łosiewicz B; (2022) Effect of amorphous calcium phosphate coatings on tribological properties of titanium grade 4 in protein-free artificial saliva. Biotribology 32, 100219. **DOI:**10.1016/j.biotri.2022.100219

[7] Osak P, Maszybrocka J, Zubko M, Rak J, Bogunia S, Łosiewicz B; (2021) Influence of sandblasting process on tribological properties of titanium grade 4 in artificial saliva for dentistry applications. *Materials 14, 7536*. DOI:10.3390/ma14247536

[8] Łosiewicz B, Osak P, Maszybrocka J, Kubisztal J, Bogunia S, Ratajczak P, Aniołek K; (2021) Effect of temperature on electrochemically assisted deposition and bioactivity of CaP coatings on CpTi grade 4. *Materials 14, 5081*. DOI:10.3390/ma14175081

[9] Osak P, Maszybrocka J, Kubisztal J, Ratajczak P, Łosiewicz B; (2021) Long-term assessment of the in vitro corrosion resistance of biomimetic ACP coatings electrodeposited from an acetate bath. *J Funct Biomater 12, 12*. DOI:10.3390/jfb12010012

[10] Łosiewicz B, Osak P, Maszybrocka J, Kubisztal J, Stach S; (2020) Effect of autoclaving time on corrosion resistance of sandblasted Ti G4 in artificial saliva. *Materials 13, 4154*. DOI:10.3390/ma13184154

[11] Primozic J, Hren M, Mezeg U, Legat A; (2022) Tribocorrosion susceptibility and mechanical characteristics of as-received and long-term in-vivo aged nickel-titanium and stainless-steel archwires. *Materials 15, 1427*. DOI:10.3390/ma15041427

[12] Achitei DC, Baltatu MS, Vizureanu P, Sandu AV, Benchea M, Istrate B; (2022) Ni-Cr alloys assessment for dental implants suitability. *Appl Sci 12, 12814*. DOI:10.3390/app122412814

[13] Dudek K, Dulski M, Łosiewicz B; (2020) Functionalization of the NiTi shape memory alloy surface by HAp/$SiO_2$/Ag hybrid coatings formed on $SiO_2$-$TiO_2$ glass interlayer. *Materials 13, 1648*. DOI:10.3390/ma13071648

[14] Osak P, Łosiewicz B; (2018) EIS study on interfacial properties of passivated Nitinol orthodontic wire in saliva modified with Eludril® mouthwash. Prot Met Phys Chem Surf 54(4), 680–688. DOI:10.1134/S2070205118040226

[15] Freitag M, Łosiewicz B, Goryczka T, Lelątko J; (2012) Application of EIS to study the corrosion resistance of passivated NiTi shape memory alloy in simulated body fluid. Solid State Phenom 183, 57–64. DOI:10.4028/www.scientific.net/SSP.183.57

[16] Lelątko J, Goryczka T, Wierzchoń T, Ossowski M, Łosiewicz B, Rówiński E, Morawiec H; (2010) Structure of low temperature nitrided/oxidized layer formed on NiTi shape memory alloy. Solid State Phenom 163, 127–130. DOI:10.4028/www.scientific.net/ssp.163.127

[17] Łosiewicz B, Skwarek S, Stróż A, Osak P, Dudek K, Kubisztal J, Maszybrocka J; (2022) Production and characterization of the third-generation oxide nanotubes on Ti-13Zr-13Nb alloy. *Materials 15, 2321*. DOI:10.3390/ma15062321

[18] Aniołek K, Łosiewicz B, Kubisztal J, Osak P, Stróż A, Barylski A, Kaptacz S; (2021) Mechanical properties, corrosion resistance and bioactivity of oxide layers formed by isothermal oxidation of Ti-6Al-7Nb alloy. *Coatings 11, 505*. DOI:10.3390/coatings11050505

[19] Łosiewicz B, Stróż A, Osak P, Maszybrocka J, Gerle A, Dudek K, Balin K, Łukowiec D, Gawlikowski M, Bogunia S; (2021) Production, characterization and application of oxide nanotubes on Ti–6Al–7Nb alloy as a potential drug carrier. Materials 14, 6142. DOI:10.3390/ ma14206142

[20] Stróż A, Dercz G, Chmiela B, Łosiewicz B; (2019) Electrochemical synthesis of oxide nanotubes on biomedical Ti13Nb13Zr alloy with potential use as bone implant. AIP Conf Proc 2083, 030004. DOI:10.1063/1.5094314

[21] Stróż A, Łosiewicz B, Zubko M, Chmiela B, Balin K, Dercz G, Gawlikowski M, Goryczka T; (2017) Production, structure and biocompatible properties of oxide nanotubes on Ti13Nb13Zr alloy for medical applications. Mater Charact 132, 363–372. DOI:10.1016/j.matchar.2017.09.004

[22] Stróż A, Dercz G, Chmiela B, Stróż D, Łosiewicz B; (2016) Electrochemical formation of second generation $TiO_2$ nanotubes on Ti13Nb13Zr alloy for biomedical applications. Acta Phys Pol 130, 1079–1080. DOI:10.12693/APhysPolA.130.1079

[23] Smołka A, Dercz G, Rodak K, Łosiewicz B; (2015) Evaluation of corrosion resistance of nanotubular oxide layers on the Ti13Zr13Nb alloy in physiological saline solution. Arch Metall Mater 60(4), 2681–2686. DOI:10.1515/amm-2015–0432

[24] Szklarska M, Dercz G, Simka W, Łosiewicz B; (2014) A.c. impedance study on the interfacial properties of passivated Ti13Zr13Nb alloy in physiological saline solution. Surf Interface Anal 46(10–11), 698–701. DOI:10.1002/sia.5383

[25] Smołka A, Rodak K, Dercz G, Dudek K, Łosiewicz B; (2014) Electrochemical formation of self-organized nanotubular oxide layers on Ti13Zr13Nb alloy for biomedical applications. Acta Phys Pol 125(4), 932–935. DOI:10.12693/APhysPolA.125.932

[26] Padrós R, Giner-Tarrida L, Herrero-Climent M, Punset M, Gil FJ; (2020) Corrosion resistance and ion release of dental prosthesis of CoCr obtained by CAD-CAM milling, casting and laser sintering. *Metals 10, 827*. DOI:10.3390/met10060827

[27] Uriciuc WA, Boșca AB, Băbțan AM, Vermeșan H, Cristea C, Tertiș M, Păscuță P, Borodi G, Suciu M, Barbu-Tudoran L, Popa CO, Ilea A; (2022) Study on the surface of cobalt-chromium dental alloys and their behavior in oral cavity as cast materials. *Materials 15, 3052*. DOI:10.3390/ma15093052

[28] Kajzer W, Szewczenko J, Kajzer A, Basiaga M, Jaworska J, Jelonek K, Nowińska K, Kaczmarek M, Orłowska A; (2021) Physical properties of electropolished CoCrMo alloy coated with biodegradable polymeric coatings releasing heparin after prolonged exposure to artificial urine. *Materials 14, 2551*. DOI:10.3390/ma14102551
[29] Mace A, Khullar P, Bouknight C, Gilbert JL; (2022) Corrosion properties of low carbon CoCrMo and additively manufactured CoCr alloys for dental applications. Dent Mater 38(7), 1184–1193. DOI:10.1016/j.dental.2022.06.021
[30] Avcu E, Baştan FE, Abdullah HZ, Ur Rehman MA, Yıldıran Avcu Y, Boccaccini AR; (2019) Electrophoretic deposition of chitosan-based composite coatings for biomedical applications: a review. Prog Mater Sci 103, 69–108. **DOI:**10.1016/j.pmatsci.2019.01.001
[31] Szulc M, Lewandowska K; (2023) Biomaterials based on chitosan and its derivatives and their potential in tissue engineering and other biomedical applications—a review. *Molecules 28, 247*. **DOI:**10.3390/molecules28010247
[32] Raafat D, Sahl HG; (2009) Chitosan and its antimicrobial potential - a critical literature survey. Microb Biotechnol 2(2), 186–201. **DOI:**10.1111/j.1751–7915.2008.00080.x
[33] Kumar-Krishnan S, Prokhorov E, Hernández-Iturriaga M, Mota-Morales JD, Vázquez-Lepe M, Kovalenko Y, Sanchez IC, Luna-Bárcenas G; (2015) Chitosan/silver nanocomposites: Synergistic antibacterial action of silver nanoparticles and silver ions. Eur Polym J 67, 242–251. **DOI:**10.1016/j.eurpolymj.2015.03.066
[34] Jiang Wang-ZhanW.Z. WZ, Cai YangY. Y, Li Hao-YingH.Y. HY; (2017) Chitosan-based spray-dried mucoadhesive microspheres for sustained oromucosal drug delivery. Powder Technol 312, 124–132. **DOI:**10.1016/j.powtec.2017.02.021
[35] Simchi A, Pishbin F, Boccaccini AR; (2009) Electrophoretic deposition of chitosan. Mater Lett 63(26), 2253–2256. **DOI:**10.1016/j.matlet.2009.07.046
[36] Szklarska M, Łosiewicz B, Dercz G, Maszybrocka J, Rams-Baron M, Stach S; (2020) Electrophoretic deposition of chitosan coatings on the Ti15Mo biomedical alloy from a citric acid solution. RSC Adv 10(23), 13386–13393. **DOI:**10.1039/d0ra01481h
[37] Kowalski P, Łosiewicz B, Goryczka T; (2015) Deposition of chitosan layers on NiTi shape memory alloy. Arch Metall Mater 60(1), 171–176. **DOI:**10.1515/amm-2015–0027
[38] Łosiewicz B, Dercz G, Szklarska M, Simka W, Łężniak M, Krząkała A, Swinarew A; (2013) Characterization of electrophoretically deposited chitosan coatings on Ti13Zr13Nb alloy for biomedical applications. Solid State Phenom 203–204, 212–215. **DOI:**10.4028/www.scientific.net/ssp.203–204.212
[39] Vokhidova NR, Ergashev KH, Rashidova SSh; (2022) Synthesis and application of chitosan hydroxyapatite: a review. Prog Chem Appl Chitin Deriv 27, 5–34. **DOI:**10.15259/PCACD.27.001
[40] Hasnain MS, Beg S, Nayak AK; (2021) Chitosan in Drug Delivery. 1st ed, Elsevier Science, Berlin, Germany.
[41] Nuc Z, Dobrzycka-Krahel A; (2021) From chitin to chitosan – a potential natural antimicrobial agent. Prog Chem Appl Chitin Deriv 26, 23–40. **DOI:**10.15259/PCACD.26.003
[42] Łosiewicz B, Popczyk M, Szklarska M, Smołka A, Osak P, Budniok A; (2015) Application of the scanning Kelvin probe technique for characterization of corrosion interfaces. Solid State Phenom 228, 369–382. **DOI:**10.4028/www.scientific.net/ssp.228.369
[43] ISO 10271:2021–02: Dentistry - Corrosion test methods for metallic materials.
[44] Lasia A; (2014) Electrochemical Impedance Spectroscopy and Its Applications. Springer, New York. **DOI:**10.1007/978–1-4614–8933–7
[45] Eco Chemie BV; (2001) User Manual for Frequency Response Analysis (FRA) for Windows Version 4.9. Eco Chemie BV, Utrecht.